



Numerical predictions of the flow around a profiled casing equipped with passive flow control devices

Costin Ioan Coșoiu, Andrei Mugur Georgescu*, Mircea Degeratu, Dan Hlevca

Technical University of Civil Engineering Bucharest, Hydraulics and Environmental Protection Department, Bucharest, Romania

ARTICLE INFO

Article history:

Received 30 December 2011

Received in revised form

15 December 2012

Accepted 22 December 2012

Available online 4 February 2013

Keywords:

Passive flow control

Profiled case

Wind energy

Flow separation

CFD

Coanda effect

ABSTRACT

The aim of this study is to optimize the shape of a casing for a small wind turbine. The optimization is performed to augment the airflow in the active transversal circular section in which the turbine rotor will be mounted. The axial length of the case was constrained. To increase the volumetric flow through the casing, we equipped the casing with passive flow control devices (i.e., circular injection slots) that operate by the overlapping of multiple aerodynamic effects. This research was conducted using numerical simulations as an investigational tool, and experimental tests performed in the wind tunnel showed that the computed results are reasonably verified by the experimental data. Furthermore, the flow mechanism around the case is better understood via the numerical data post-processing. In this investigation, a total of 13 shapes of the casing were tested, and the results suggest that the optimal variant ensures a maximum axial velocity increase in the active transversal section of the casing by a factor of up to 3.25.

© 2013 Published by Elsevier Ltd.

1. Introduction

Modern wind turbines produce energy efficiently from mean wind speeds of 7 m/s or greater. In areas where the wind frequently blows at lower speeds, the energy from wind turbines cannot be as efficiently collected using classical means. In Romania, for example, the frequency distribution of the wind speed occurrence has a maximum in the lower velocity region, approximately 5 m/s, for more than 70% of this country's territory. The aerolian potential is also weak because the amount of specific energy, computed in terms of energy divided by square meter, is rather low for the majority of the available sites (Degeratu et al., 2003).

Wind can be concentrated by using ducted turbines, which in principle consist of a classical wind turbine surrounded by a structure, with a shape given by either a simple or a more complex curve, that is revolved against the rotational axis of the turbine rotor. Unlike the case of the free rotor in which the air decelerates as it approaches the turbine, in the case of the ducted rotor (where the static pressure inside the casing is smaller than the atmospheric pressure), a suction effect is created that leads to an increase in the velocity and consequently to an increase in

power for the same surface swept by the blades. The power increase is significant for a turbine with the same rotor diameter because the power varies with the third power of the wind speed. Thus, the use of ducted rotors assures the possibility of concentrating the dispersed wind energy, even at low wind conditions, allowing for greater power output from a rotor with a given diameter.

Wind concentrators coupled with wind turbines have been used since ancient times. In Persia, vertical windmills were built using a device that diverted airflow from the half of the rotation circle where the blades give negative thrust through the half of the rotation circle where the blades give positive thrust. Thus, this structure behaved as a wind energy concentrator (Pumpelly, 1905).

Studies on the topic of flow augmentation through wind turbines have been performed since the sixth decade of the 20th century. However, this subject was not tackled by many research groups due to the high costs involved in the manufacturing of the proposed solutions. The studies performed in this area include that of Lilley and Rainbird (1956), Gilbert et al. (1978), Gilbert and Foreman (1983), Igra (1981), Phillips et al. (1999), Bet and Grassmann (2003), Abe and Ohya (2004), Abe et al. (2005), Ohya et al. (2008), Ohya et al. (2011), Matsushima et al. (2006), and Wang et al. (2008).

Several concepts have emerged from these studies. The first concept implies a convergent-divergent nozzle type aerolian concentrator (Lilley and Rainbird, 1956; Wang et al., 2008), with a long diffuser, located downstream of the active transversal

* Correspondence to: Technical University of Civil Engineering Bucharest, Hydraulics and Environmental Protection Department, B-dul Lacul Tei, Nr. 124, Sector 2, 020396 Bucharest, Romania. Tel.: +40 212433660.

E-mail addresses: andreig@hidraulica.utcb.ro, andrei_georgescu2003@yahoo.com (A.M. Georgescu).

Nomenclature

D	casing throat diameter	l_∞	turbulent length scale at the inlet
L	casing axial length	k_∞	turbulent kinetic energy at the inlet
c	chord length of the profile	ω_∞	specific dissipation rate of turbulent kinetic energy at the inlet
ρ	density	y^+	dimensionless wall distance
\bar{p}	mean static pressure	x	axial coordinate
\bar{u}_i	mean velocity	r	radial coordinate
\bar{u}_i'	mean turbulent velocity fluctuation	\bar{p}_i	mean value for static pressure in the i section
ν	kinematic viscosity	\bar{p}_{di}	mean value for dynamic pressure in the i section
k	turbulent kinetic energy	\bar{p}_{ti}	mean value for total pressure in the i section
ω	specific dissipation rate of turbulent kinetic energy	A_i	transversal area in the i section
Γ_k	effective diffusivity of k	C_p	pressure coefficient
\tilde{G}_k	generation of turbulent kinetic energy due to mean velocity gradients	C_{ps}	static pressure coefficient
Y_k	dissipation of k due to turbulence	C_{pd}	dynamic pressure coefficient
Γ_ω	effective diffusivity of ω	C_{pt}	total pressure coefficient
Y_ω	dissipation of ω due to turbulence	p_∞	static pressure in the free stream
D_ω	cross diffusion term	Q	the volumetric flow
u_∞	velocity in the free stream	D_m	model diameter
I	turbulent intensity	Re_m	Reynolds number computed with model diameter
		p	local pressure
		u	local velocity magnitude

section, that gradually recovers the static pressure against the kinetic term (Lilley and Rainbird, 1956). Another concept was centered on a casing produced with injection slots for boundary layer separation control and a large angle for the diffuser located downstream of the throat (Gilbert et al., 1978; Gilbert and Foreman, 1983; Igra, 1981; Phillips et al., 1999). A third concept involved a ring-wing type wind concentrator (Bet and Grassmann, 2003). This last concept is much simpler in terms of the shape complexity of the casing because it uses a different mechanism to increase the flow through the active section of the duct. The casing is a diffuser type with a vertical circular flange attached at the exit section (Abe and Ohya, 2004; Abe et al., 2005; Ohya et al., 2008; Matsushima et al., 2006). This flange ensures the optimal conditions for boundary layer separation at the free edge, creating a pair of vortices that travel downstream following a pattern similar to von Karman's vortex street. This effect implies a strong decrease in the static pressure downstream of the turbine and thus implicitly, larger airflow through the diffuser. An updated version of this concept was also developed for use with larger diameter turbine rotors, featuring a diffuser with a shorter length (Ohya et al., 2011).

Considering these concepts, we conclude that the increase in the volumetric flow rate through the throat of the concentrator may be achieved by overlapping of several aerodynamic effects, each derived from one of the specific constructive solutions previously presented. The solutions adopted in our study, together with their respective aerodynamic effects, include:

1. A casing with the interior profile of a convergent-divergent nozzle in conjunction with a concentration effect that leads to air acceleration in the duct and assures a higher mean velocity in the nozzle throat followed by a gradual recovery of the kinetic energy in the flared section.
2. A ring-wing casing type based on an airfoil with high lift and an efficient lift-to-drag ratio that assures an intensification of the flow on the upper part through the casing due to induced circulation around these airfoil types (Oertel, 2010).
3. Provision of a circular slot assembly that connects the lower part with the upper part of the airfoil, i.e., the higher pressure on the exterior of the casing with the lower pressure at the

interior. The circular slots are designed to ensure air injection into the boundary layer to energize the flow and delay its separation. The pressure losses are also reduced, ensuring an increase of the volumetric flow rate that passes through the duct.

4. Assurance of a high divergence angle of the nozzle, which leads to flow separation at the trailing edge of the casing and provides a lower pressure in the downstream wake. The low-pressure zone provides the necessary conditions for the volumetric flow rate increase through the minimal section of the casing. A lower ratio between the throat section of the casing and the exit cross-section ensures a higher volumetric flow through the turbine. In this respect, the exit diameter was not altered in the optimization process. The nozzle with a high downstream flare works as a yaw system due to the high pressure differences that occur on different areas of the exterior casing surface, (i.e., those facing the wind).

In this paper, we propose a casing that includes all of the favorable effects generated by the above mentioned solutions. The solutions were implemented on an existing casing (Coşoiu et al., 2011). The turbine placed inside the casing consists of a small domestic horizontal axis turbine with a rated power of 1 kW and a diameter of 2.272 m. The existing casing represents the initial geometry of the concentrator and will be denoted as $v-1$ in the following paragraphs.

The $v-1$ casing was obtained by rotation around the turbine axis (over 360°) of a NACA4412 wing profile with an incidence angle of 10° . The resulting profile is a ring-wing type that intensifies the flow on the pressure side of the airfoil and thus increases the flow through the casing due to induced circulation around the airfoil. In addition, the interior profile of the casing becomes a convergent-divergent nozzle, leading to air acceleration in the throat. The distance from the rotation axis was chosen such that the diameter of the throat enables the mounting of a turbine rotor with $D=0.44c$ in the concentrator (with c as the chord length of the profile).

To ensure an even greater divergence angle, starting from $0.8c$, the NACA4412 profile was modified so that the incidence angle of the trailing edge becomes 30° . As mentioned above, a high divergence angle at the trailing edge leads to the flow separation

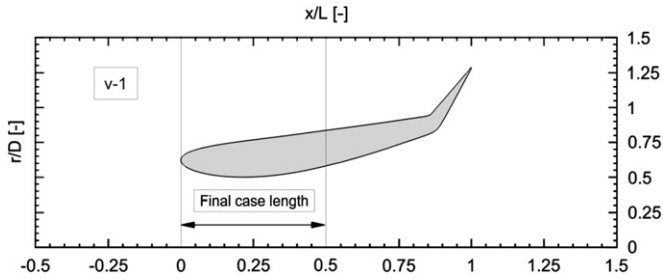


Fig. 1. Initial case denoted as *v-1*.

that provides a lower pressure in the wake and an implicit increase of the flow rate through the nozzle. After modifying the profile, the axial length of the casing becomes $L=2.09D$. The ratio between the area of the throat and the area of the exit cross-section is equal to 0.15. The modified airfoil that generates the initial case *v-1* is shown in Fig. 1.

One of the constraints imposed upon the optimized casing is that its length should be equal to half of the length of the *v-1* case. This dimensional reduction is necessary to properly apply the concept of ducting in the wind turbines with larger rotor diameters. In these cases, the wind loads and the weight of the unit may pose severe constraints (Ohya et al., 2011).

Another imposed constraint was that the flow rate through the optimized casing should be greater than or equal to that of the *v-1* case. To cope with this constraint, we have introduced circular slots for air injection from the pressure side to the suction side of the profile using a step-by-step procedure. This air injection re-energizes the boundary layer on the interior of the nozzle and thus delays its separation. By using this procedure, the separation point was successively shifted downstream.

The optimization procedure is solely based on the numerical results obtained from 2D axisymmetric models of the casing. The numerical method was verified using a well-documented test case similar to our study from the literature (Burt, 1994). In the numerical simulations, no turbine rotor was mounted inside the nozzle. The introduction of an axial rotor would have compromised the axial symmetry hypothesis and would have led to more time-consuming 3D numerical simulations. The step-by-step procedure used to optimize the shape of the casing and the final shape that resulted from this process are presented in Section 3. The resulting shape of the casing was experimentally tested in a wind tunnel, and the results were compared to those obtained from a 2D axisymmetric numerical model with boundary conditions matching the wind tunnel test.

2. Numerical model and computational conditions

2.1. General hypothesis

The casing is defined by a volume of revolution against the axis of symmetry, and the flow is also considered symmetrical. In addition, the flow is considered to be identical in the successive radial planes. Therefore, 2D axisymmetric simulations were used. These types of simulations are frequently used to simulate swirling flow in turbo-machines and in fluid domains defined by axial symmetrical geometries (Susan-Resiga et al., 2011). In particular, this approach has produced good results for flow simulations of the air in ducts used to augment wind turbine performances (Abe and Ohya, 2004; Abe et al., 2005).

The numerical approach in this study focused on a method that allows for problem solving in a reasonably short computational time.

In the absence of the turbine rotor mounted in the active section, the flow is characterized by parameters that do not vary over time, and with this consideration, the simulations were performed in the steady state.

2.2. The turbulence model

All simulations were performed using the viscous pressure-based $k-\omega$ SST turbulence model implemented in the ANSYS FLUENT commercial software. This model uses RANS decomposition for the momentum and continuity equations as follows:

$$\frac{\partial \bar{u}_i}{\partial x_i} = 0 \quad (1)$$

$$\bar{u}_j \frac{\partial \bar{u}_i}{\partial x_j} = -\frac{1}{\rho} \frac{\partial \bar{p}}{\partial x_i} + \frac{\partial}{\partial x_j} \left[v \left(\frac{\partial \bar{u}_i}{\partial x_j} + \frac{\partial \bar{u}_j}{\partial x_i} \right) - \bar{u}_i' \bar{u}_j' \right] \quad (2)$$

where ρ , \bar{p} , \bar{u}_i , \bar{u}_i' and v denote the density, the mean static pressure, the mean velocity, the mean turbulent velocity fluctuations and the kinematic viscosity, respectively. In Eq. (2), no exterior forces are taken into account considering the hypothesis presented in the previous subsection.

The closure problem is solved using the Boussinesq hypothesis to model the Reynolds stresses. This approach implies only two additional equations to be solved instead of five (for 2D simulations such as the ones presented in this study). Thus, the turbulent viscosity is computed by introducing two additional transport equations for the turbulence kinetic energy (k) and its specific dissipation rate (ω) (Menter, 1994):

$$\frac{\partial}{\partial x_i} (k \bar{u}_i) = \frac{1}{\rho} \left[\frac{\partial}{\partial x_j} \left(\Gamma_k \frac{\partial k}{\partial x_j} \right) + \tilde{G}_k - Y_k \right] \quad (3)$$

$$\frac{\partial}{\partial x_i} (\omega \bar{u}_i) = \frac{1}{\rho} \left[\frac{\partial}{\partial x_j} \left(\Gamma_\omega \frac{\partial \omega}{\partial x_j} \right) + G_\omega - Y_\omega + D_\omega \right] \quad (4)$$

where Γ_k , \tilde{G}_k , Y_k , Γ_ω , G_ω , Y_ω and D_ω denote the effective diffusivity of k , the generation of turbulent kinetic energy due to the mean velocity gradients, the dissipation of k due to turbulence, the effective diffusivity of ω , the generation of ω , the dissipation of ω due to turbulence and the cross-diffusion term, respectively (ANSYS Inc., 2010).

The RANS approach yields a more robust method that, when combined with the assumption of steady 2D axisymmetric flow conditions, gives fast results that are immediately used in the optimization process for the casing shape. Moreover, the $k-\omega$ SST turbulence model produced good results for the prediction of flow separation under adverse pressure gradients (Bardina et al., 1997). In our study, the flow separation under adverse pressure gradients is present at the interior of the casing, and therefore, we considered the $k-\omega$ SST turbulence model as appropriate.

A similar approach using a RANS formulation in terms of a $k-\omega$ turbulence model (a modified ABL- ω model) was taken by Abe and Ohya (2004) to study the flow fields around flanged diffusers, with good results that were verified by experiments.

For the simulations, second-order discretization schemes were used for pressure, the momentum equation and the transport equations for the specific turbulence model parameters. The pressure-velocity coupling was achieved through a coupled algorithm. Considering the fact that the flow was considered as a 2D axisymmetric steady flow, all of the equations that must be solved are written in a cylindrical representation in a stationary reference frame.

2.3. Grid and computational conditions

The computational domain was constructed such that the distances between the domain inlet and the inlet transversal

section of the casing, the outlet transversal section of the casing and the outlet of the domain are equal to 11 casing lengths. The maximum distance between the axis of rotation (i.e., the lower boundary) and the upper boundary is equal to five diameters of the minimum cross-section of the interior nozzle. The blockage is therefore less than 5%.

At the inlet boundary, the axial velocity (u_∞) was set to a constant value of 3.5 m/s, corresponding to notably low wind conditions. Therefore, the Reynolds number that characterizes the flow was 5.4×10^5 , written with the throat diameter (D) and the free stream velocity ($Re = u_\infty D / \nu$). The turbulence kinetic energy (k_∞) and its specific dissipation rate (ω_∞) were computed indirectly (ANSYS Inc., 2010) by specifying the turbulence intensity (I_∞) and the turbulence length scale (l_∞) according to the formulae:

$$k_\infty = \frac{3}{2} (u_\infty I_\infty)^2 \quad (5)$$

$$\omega_\infty = \frac{k_\infty^{1/2}}{C_\mu^{1/4} l_\infty} \quad (6)$$

where C_μ is an empirical constant specified in the turbulent model and equal to 0.09.

Considering the characteristics of the natural wind (Davenport et al., 1980) at the inlet boundary, the turbulence intensity (I_∞) was set to a constant value of 0.2. The turbulence length scale (l_∞) was set to 5.86 m, equal to the largest transversal obstacle in the flow (i.e., the diameter of the exit cross-section of the casing).

At the outlet boundary, the pressure (p_e) was set to 0 gauge scale. No slip conditions were specified for all of the solid boundaries. The upper boundary was set as a zero shear slip wall. Details regarding the computational domain and boundary conditions are presented in Fig. 2.

The $k-\omega$ SST turbulence model has the advantage of correctly solving the flow in the boundary layer without being sensitive to k and ω values outside the shear layer, as in a classical $k-\omega$ formulation. The model switches to a $k-\varepsilon$ formulation due to the blending functions that are included in the Γ_k , Γ_ω , G_ω and D_ω terms in Eqs. (3) and (4). In the viscous sub-layer, this turbulence model is capable of predicting the flow parameters without the use of wall functions.

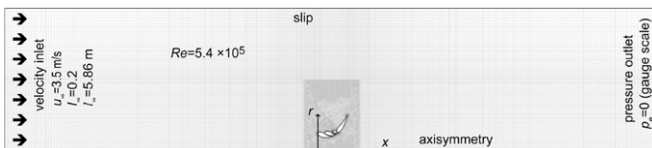


Fig. 2. Grid and boundary conditions: $v11$ case (see Section 3 for details).

This approach required refinement of the grid in the near wall region to correctly simulate the flow. We also performed a grid dependency test to determine the best approach for the mesh generation procedure. In this work, we present the results of the tests for the $v11$ case (see Section 3 for details).

Three different grids were used with 70,000, 130,000 and 220,000 cells, and the Reynolds number was 5.4×10^5 . The meshes were of structured–unstructured mixed types, created using quad cells and refined in the area of the flow adjacent to the casing by implementing the size functions in the pre-processing phase. Additionally, in the pre-processing phase, we used region adaption to refine the grid for the meshes with 130,000 and 220,000 cells. For the 130,000-cell mesh, we used the region adaption around the case only while for the 220,000-cell mesh we used region adaption across the entire domain.

In the processing phase, we adapted the grid at the boundary to achieve $y^+ \approx 1$ for the larger meshes (130,000 and 220,000 cells).

The pressure coefficients and dimensionless axial velocities along the axis of the nozzle are plotted in Fig. 3. For the meshes constructed with the $y^+ \approx 1$ adaption, the differences between the values are quite small. For the grid with no adaption, the results differ substantially. The differences are explained by the rough resolution of the mesh in the region around the casing, especially near the walls where the $y^+ \approx 1$ condition is required by the low Reynolds number turbulence model that we adopted in our numerical study.

For all of the cases presented in our study, the meshes were generated using the same procedure as that applied for the 220,000-cell grid. The resulting cell numbers were approximately 200,000, with variations depending on the simulation.

2.4. Numerical method validation: the AGARD A2 experiment

Prediction of the flow around the multi-element airfoil has posed certain difficulties for CFD codes and the turbulence-modeling community (Rumsey et al., 1998; Morrison, 1998). The study presented in this paper investigates a flow that has similar characteristics, and thus it is important to determine whether the numerical investigation method is capable of generating correct predictions.

The performed mesh convergence study itself does not guarantee a physically correct solution. To obtain greater confidence in the numerical simulation results, we performed a numerical study on a test case that presents similar characteristics to the case investigated in this study, i.e., flow through narrow passages between airfoil-like surfaces with separation. We chose the high-lift airfoil investigated in the AGARD A2 experiment (Burt, 1994), an experiment specifically performed for CFD code validation that

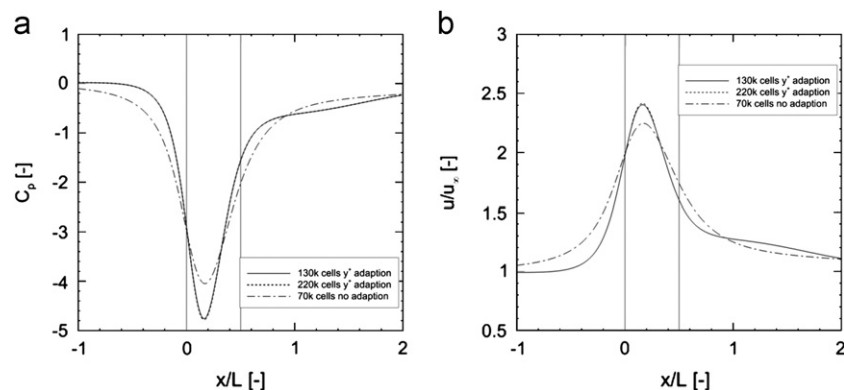


Fig. 3. Comparison of on-axis distribution: (a) pressure coefficient and (b) dimensionless axial velocity.

was deployed in the early 1970s and used as a code validation challenge by the CFD Society of Canada (Fejtek, 1997).

The high-lift airfoil, called NHLP-2D, represents a typical three-element take-off configuration consisting of a slat, the main element and a flap. The slat is positioned at an angle of 25° while the flap has a deflection angle of 20° . Narrow passages are located between these three elements that direct the air at its upper part to generate the high lift.

The AGARD A2 experiment was performed at two angles of attack: 4.01° and 20.18° . Previous numerical studies (Rumsey et al., 1998) have shown that for the second angle of attack configuration, modeling of the wind tunnel walls has a large effect on the simulation results. In our numerical setup procedure, because the far boundary aligned with the flow has an attached slip condition and is positioned at a sufficient distance from the model, we performed the study only for the 4.01° angle of attack configuration.

The flow is identical in the parallel transversal planes such that the 2D space dimension hypothesis is also similar. Because the NHLP-2D experimental model consists of a two-dimensional wing with high-lift devices, the axisymmetrical hypothesis does not apply to this case. The computational domain and the grid were generated using the method described in Section 2.3, producing a grid with 360,000 cells. At the inlet boundary condition, the velocity (u_∞) was set such that the Reynolds number based on the stowed-geometry chord was equal to 3.52×10^6 . On the outlet boundary, the pressure (p_e) was set to 0 gauge scale.

The parameters monitored during the experiments were the pressure coefficient ($C_p = (P - P_\infty) / (0.5 \rho u_\infty^2)$) distributions on the elements of the high-lift airfoil and the total pressure coefficient ($C_{pt} = (p_t - p_\infty) / (0.5 \rho u_\infty^2)$) profiles in the boundary layer located on the upper surface at four stations, with one on the main element ($x/c = 0.35$) and three on the flap ($x/c = 0.91$, $x/c = 1.066$ and

$x/c = 1.214$). Fig. 4 presents the NHLP-2D profile and the location of the total pressure profiles.

Fig. 5 shows that the pressure coefficient distributions are well fitted to the experimental data, especially on the main element, the flap and the upper part of the slat. The numerical simulation results differ somewhat from the experimental results on the cove region of the slat. This was also observed in earlier CFD simulations on the same case (Rumsey et al., 1998; Morrison, 1998).

For the total pressure coefficient profiles in the boundary layer (Fig. 6), the numerical simulation results show the same trend and are in agreement with the experimental data. The wake from the slat is observed at the station placed on the main element, and the main element wake is well emphasized on the flap. However, for the profiles computed at the stations placed on the flap, the numerical simulation predicts a curve that is shifted slightly downward as compared to the experimental points. The wake defect is more noticeable at the second station on the flap. On the main element, there are no large differences between the numerical and experimental results.

The differences in the wake prediction can be explained by the deficiencies in the transition prediction on the generating element of the wake (Rumsey et al., 1998). The turbulence model used in this work is not capable of modeling the transition process, and thus, the flow in the boundary layer in the wake of the main element is not accurately computed. However, the flow itself is highly complex, and the 2D space dimension hypothesis used in the simulation removes the possibility of predicting additional 3D effects that could appear in the real experiment.

Although certain variations exist, the proposed numerical method is suitable for use in our shape optimization study. The inviscid effects are well predicted, but for the viscous state, an extra experimental investigation may be imposed.

3. Numerical investigation procedure

The shape of the casing equipped with a passive flow control device resulted at the end of an iterative heuristic optimization process. The procedure consisted of a step-by-step iteration involving several stages as described below:

Step 0. First, an initial shortened casing denoted as $\nu 0$ was created with an axial length equal to one half of the $\nu-1$

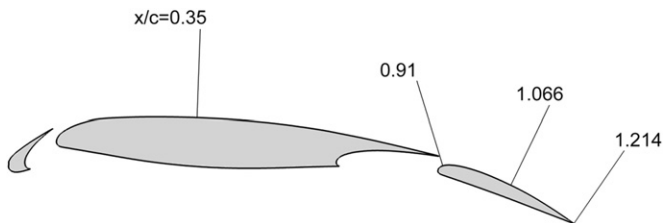


Fig. 4. Location of total pressure profiles for NHLP-2D three-element high-lift airfoil.

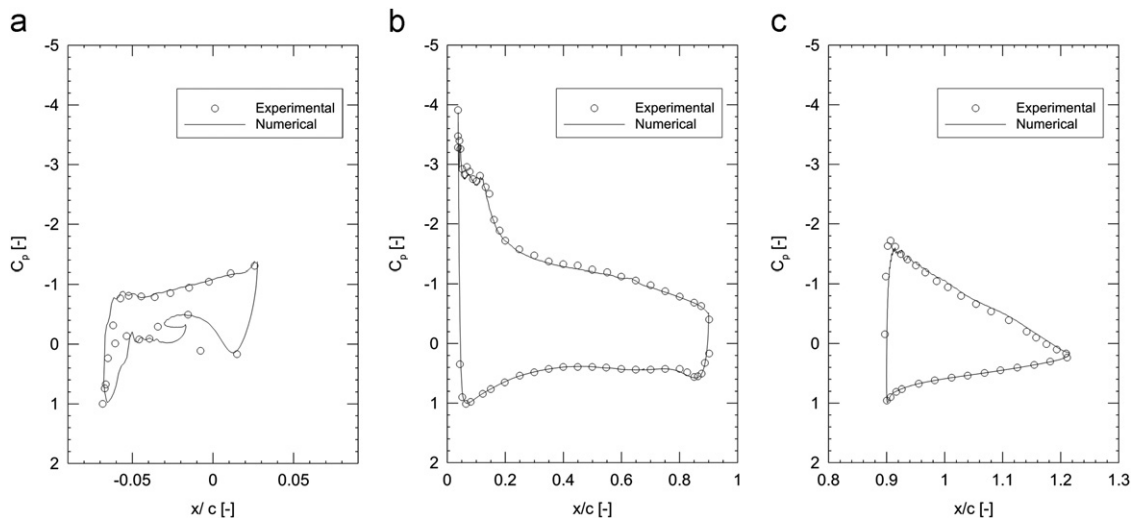


Fig. 5. Pressure coefficient distributions on the surface of the NHLP-2D three-element high-lift airfoil. Experimental vs. numerical simulations comparisons: (a) slat, (b) main element and (c) flap.

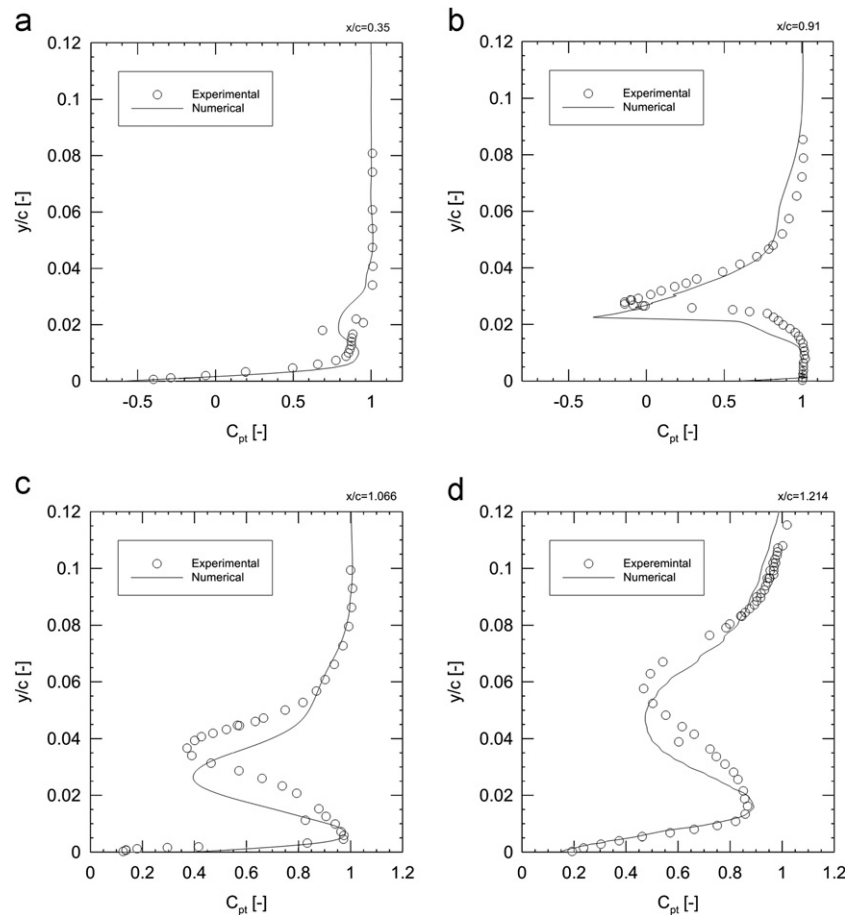


Fig. 6. Total pressure coefficient profiles for the NHLP-2D three-element high-lift airfoil: (a) $x/c=0.35$, (b) $x/c=0.91$, (c) $x/c=1.066$ and (d) $x/c=1.214$.

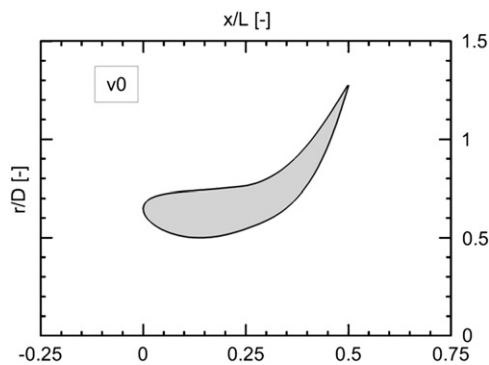


Fig. 7. Initial shortened version denoted v_0 .

version and with an identical ratio between the throat area and exit cross-section (Fig. 7). The contour of the $v-1$ geometry was partially preserved. In the optimization procedure, this version is designated as the initial *parent case*.

Step 1. A numerical simulation was performed on the *parent case* with the computational conditions described in Section 2. This simulation enabled us to identify the separation point at the interior of the *parent casing*. The identification was performed by inspecting both the streamlines and the values of the wall shear stress around the casing (the shear stress should be 0 at the separation point).

Step 2. A new *child case* was constructed starting from the *parent case* geometry. The interior separation point and selected higher-pressure exterior points on the casing were

connected using a ring channel. This connection was expected to move the separation point downstream due to the exterior air injection that re-energizes the flow.

Step 3. A numerical simulation was performed on the *child case* with the computational conditions described in Section 2. This simulation enables us to quantify the performance of the *child casing*.

Step 4. For the selected *child case*, several aspects were taken into account in the selection process:

First, we investigated the displacement of the flow separation point downstream of the nozzle of the *child case* with respect to the separation point of the *parent*. The separation point position affects the pressure losses in the casing and the fluid boundaries of the main interior flow.

Second, we computed the volumetric flow rate in the throat of the casing and compared it with that of the *parent casing*.

Third, we compared the dimensionless velocity magnitude and the pressure coefficient fields around the *child casing* with those from around the *parent casing* to globally identify the main flow parameters changes.

Fourth, we quantified the mean static, dynamic and total pressure variations at the interior flow in the *child casing*. In the divergent zone of the duct, the potential energy is recovered from the kinetic energy. A part of it is lost due to the flow separation at the interior of the casing. The mean values for the static pressure, the dynamic pressure and the total pressure are directly linked to the potential, the kinetic and the total energy fluxes of the flow, respectively. We compared the variation of the mean values for the static, the dynamic and the total pressure in

the casing along the flow direction between the *child* and *parent* cases.

If the performance values of the *child* case were lower than those of the *parent* case, then the entire process was reiterated starting from *Step 2* by choosing another exterior point to connect to the interior separation point.

If the performance values of the *child* case were higher than those of the *parent* case, the *child* case was selected and became a new *parent* case.

Step 5. If the performances of the new parent case were higher than those of the *v-1* casing, then this new *parent* case became the final optimized case. Otherwise, the entire process was reiterated starting from *Step 1* with additional ring slots.

The entire procedure was conducted for two (case *v5*), three (cases *v6* and *v12*) and four slots (cases *v7*, *v9*, *v10*, *v11* and *v13*). A five-slot case was also studied with inconclusive results (case *v8*). In *Table 1*, we present the key parameters of the studied casings.

In this paper, only the validated versions for one, two, three and four slots are compared, i.e., the versions denoted,

respectively as *v4*, *v5*, *v6* and *v11*. *Fig. 8* presents the geometries of the above mentioned casings.

Additional details are presented in *Section 5*.

4. Experimental investigations

Although the numerical investigation method used in this investigation performed well in similar studies, for a greater confidence in the results, basic experimental tests were also conducted for the chosen *v11* casing version (see *Section 5* for details).

The tests were performed in the Boundary Layer Wind Tunnel 2 (TASL 2) in the Hydraulic and Environmental Protection Department of the Technical University of Civil Engineering in Bucharest. The tunnel consists of a long vein open circuit wind tunnel. The airflow is controlled with a fan driven by a 37-kW electric motor with adjustable speed (continuous from 0 to 100%), and the tunnel is connected to the suction side of the fan. The TASL 2 contains two experimental zones, both with a cross-section of $1200 \times 1200 \text{ mm}^2$. The first zone, used for experiments that require a constant velocity profile, is situated upstream in the long vein near the air inlet. The second zone is situated downstream of the long vein, towards the suction side of the fan, and is used for experiments requiring a well-developed boundary layer velocity profile. In this study, the upstream experimental zone was used in which the velocity profile is uniform. The velocity (u) in the free stream was 13 m/s, corresponding to a Reynolds number (Re_m) equal to 1.01×10^5 computed with the model diameter (D_m) of 0.11 m.

To obtain a blockage lower than 5%, a 1:20 scale model of the *v11* casing was built. The model was manufactured using a 3D printer and made from a high-performance composite material. The CAD source file for printing was created in ANSYS Design Modeler. The model was divided into six parts that were assembled using an epoxy bi-component adhesive. The parts of the model before assembly are presented in *Fig. 9*.

Table 1
Key parameters of the studied casings.

No.	Name	No. of ring slots	Parent version
1	<i>v1</i>	1	<i>v0</i>
2	<i>v2</i>	1	<i>v0</i>
3	<i>v3</i>	1	<i>v0</i>
4	<i>v4</i>	1	<i>v0</i>
5	<i>v5</i>	2	<i>v4</i>
6	<i>v6</i>	3	<i>v5</i>
7	<i>v7</i>	4	<i>v6</i>
8	<i>v8</i>	5	<i>v7</i>
9	<i>v9</i>	4	<i>v6</i>
10	<i>v10</i>	4	<i>v6</i>
11	<i>v11</i>	4	<i>v6</i>
12	<i>v12</i>	3	<i>v5</i>
13	<i>v13</i>	4	<i>v12</i>

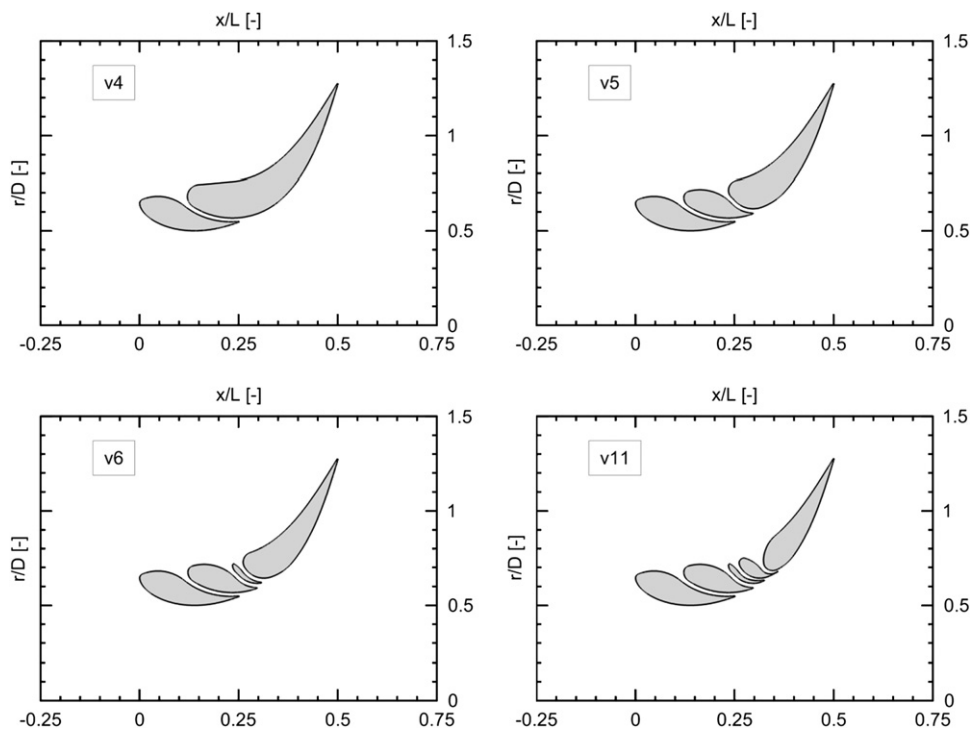


Fig. 8. The *v4*, *v5*, *v6* and *v11* casing versions.

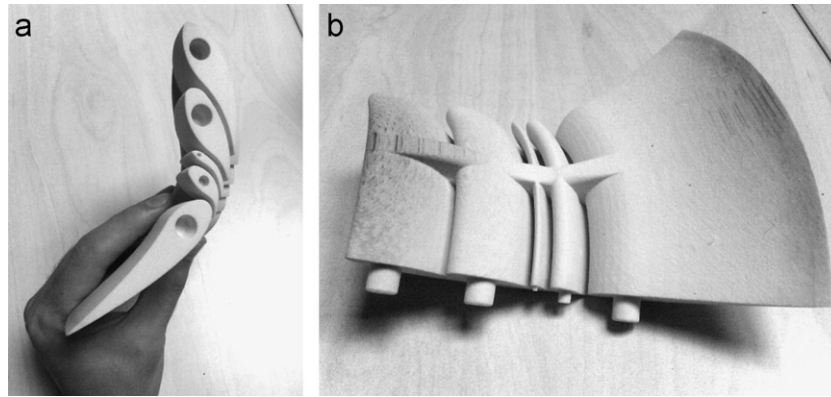


Fig. 9. The $\nu 11$ 1:20 scale experimental model before assembly: (a) lateral view and (b) overview.

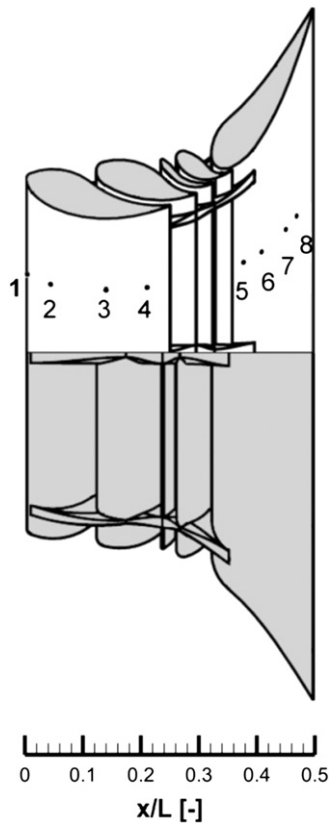


Fig. 10. The $\nu 11$ 1:20 scale experimental model: relative dimensions and pressure tap locations.

Eight pressure taps were placed on the interior surface of the casing for measurement of the pressure distributions. All of the pressure taps were placed in a radial plane, inclined at an angle of 28° with respect to the vertical, and their positions with respect to the length of the $\nu-1$ reference version of the casing are shown in Fig. 10. Four of the taps were positioned on the upstream section of the casing, before the first circular slot, and four on the downstream section, after the fourth slot. The pressure taps were manufactured after the model was assembled.

Additionally, the static pressure profile was measured along the axis of the casing. A static pressure probe mounted on a traversing mechanism able to move back and forth along the axis of the casing was used for this purpose. The traversing mechanism was digitally controlled from outside of the wind tunnel. A picture of the $\nu 11$ experimental model placed in the experimental vein of the TASL 2 wind tunnel is shown in Fig. 11.



Fig. 11. The $\nu 11$ 1:20 scale experimental model placed in the TASL 2 experimental vein. The traversing system and the static pressure probe are shown in the far plane.

A Pitôt-Prandtl tube was placed upstream of the model for computation of the pressure coefficients and located at a distance of seven axial lengths of the $\nu 11$ model.

All of the pressure taps at the interior surface, the static pressure probe placed in the axis of the casing, and the static pressure probe of the Pitôt-Prandtl tube were plugged into the low-pressure connectors of ten AutoTran model 600D-013 differential pressure transducers with a measurement range between 0 and 1270 Pa. The high-pressure connectors of the pressure transducers were connected to a common rail linked to the total pressure probe of the Pitôt-Prandtl tube (see Fig. 12).

The electrical signals from the transducers were collected by a computer using an external acquisition board. The pressure transducers were calibrated before the beginning of the experiments. At an air velocity of 0 m/s in the tunnel, the pressure transducers should transmit a voltage signal that signifies a 0 Pa pressure difference.

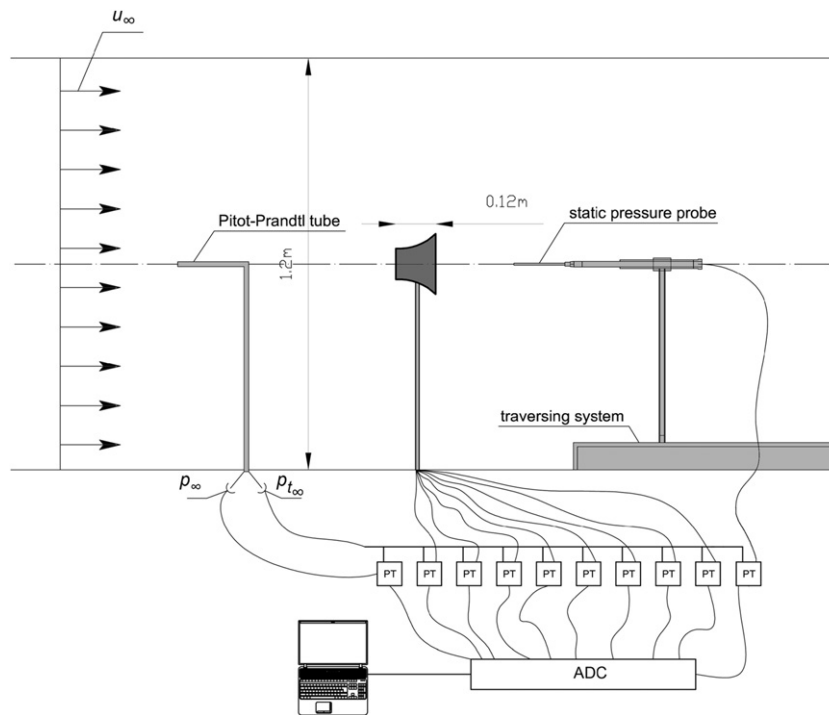


Fig. 12. Schematic diagram of the experimental setup in the wind tunnel.

Figs. 9, 10 and 11 show the stiffening ribs necessary to hold the five circular sections of the casing together. The stiffening ribs were not taken into account in any of the numerical models.

5. Results and discussion

5.1. Numerical simulations: $Re=5.4 \times 10^5$

Tests were conducted for a functioning regime characterized by a Reynolds number with a value of 5.4×10^5 as computed with the throat diameter of the actual-scale casing. This value corresponds to a wind velocity of 3.5 m/s at which we expect the turbine mounted inside the case to operate under nominal conditions. The grid, the numerical model, and the computational conditions are described in Section 2.

As previously mentioned in Section 3, we present only the selected versions for one-, two-, three- and four-injection slots, i.e., the $\nu 4$, $\nu 5$, $\nu 6$ and $\nu 11$ casing versions, respectively. The numbering of the slots begins at the throat of the nozzle and continues downstream in the flow direction.

The streamlines around the studied casing versions are presented in Fig. 13. In the investigations, several general flow patterns were identified. Two flow separation points can be observed on the interior of the duct surface. The main separation points are placed downstream of the throat, with varying locations depending on the casing version. The second separation points are identified downstream of the last injection slot for each casing version, except for the $\nu 11$ version in which the main flow is separated only once.

A pair of toroidal vortices is formed downstream of the casing due to the flow separation at the trailing edge. The characteristic length of the vortices on the axial dimension is similar to the exit cross-section diameter of the casing. The shape of the vortices is influenced by the second separation point of the main flow.

The main interior flow is bounded in part by the interior solid boundaries of the casing and downstream of the second

separation point by a fluid boundary shared with the interior toroidal vortex.

A more detailed analysis of the main flow for each casing provides supplementary information. Depending on the casing version, the energy that maintains the vortices is either drained from the main flow, drained from the secondary flow in the circular slots, or both.

For the casing version with one slot ($\nu 4$), the main flow separation occurs at $x/L \approx 0.22$ upstream of the slot. The radius of the main fluid flow boundary at $x/L \approx 0.75$ is equal to $r/D \approx 0.63$. The slot injects the air into the vortex zone, providing a good part of the energy that will be consumed by the two ring vortices. The secondary flow separation occurs at $x/L \approx 0.33$ downstream of the slot.

For the second casing configuration ($\nu 5$) with two ring slots, the main flow separation occurs at $x/L \approx 0.28$ upstream of the second slot, with the radius of the main flow at $x/L \approx 0.75$ equal to $r/D \approx 0.67$. The first slot injects the air directly into the main current, while the second slot injects into the vortex zone. Both air injections provide a part of the energy that will be dissipated in the pair of ring vortices. The secondary flow separation due to a positive pressure gradient along the flow occurs at $x/L \approx 0.35$ downstream of the second slot.

For the third version ($\nu 6$) with three ring slots, the main flow separation occurs at $x/L \approx 0.3$, i.e., upstream of the third slot, with the semi-diameter of the main flow at $x/L \approx 0.75$ equal to $r/D \approx 0.69$. The first two slots inject air into the main current, while the third slot injects air into the vortex zone, providing a major part of the energy that will be consumed by the two ring vortices. The secondary flow separation occurs at $x/L \approx 0.36$ downstream of the third slot.

In the fourth version ($\nu 11$) with four ring slots, the separation of the main flow is moved upstream of the first slot, at $x/L \approx 0.23$, but the semi-diameter of the main flow at $x/L \approx 0.75$ is substantially increased and is equal to $r/D \approx 0.74$.

The volumetric flow rate is a decisive parameter that governs the amount of available energy in the throat. We computed the

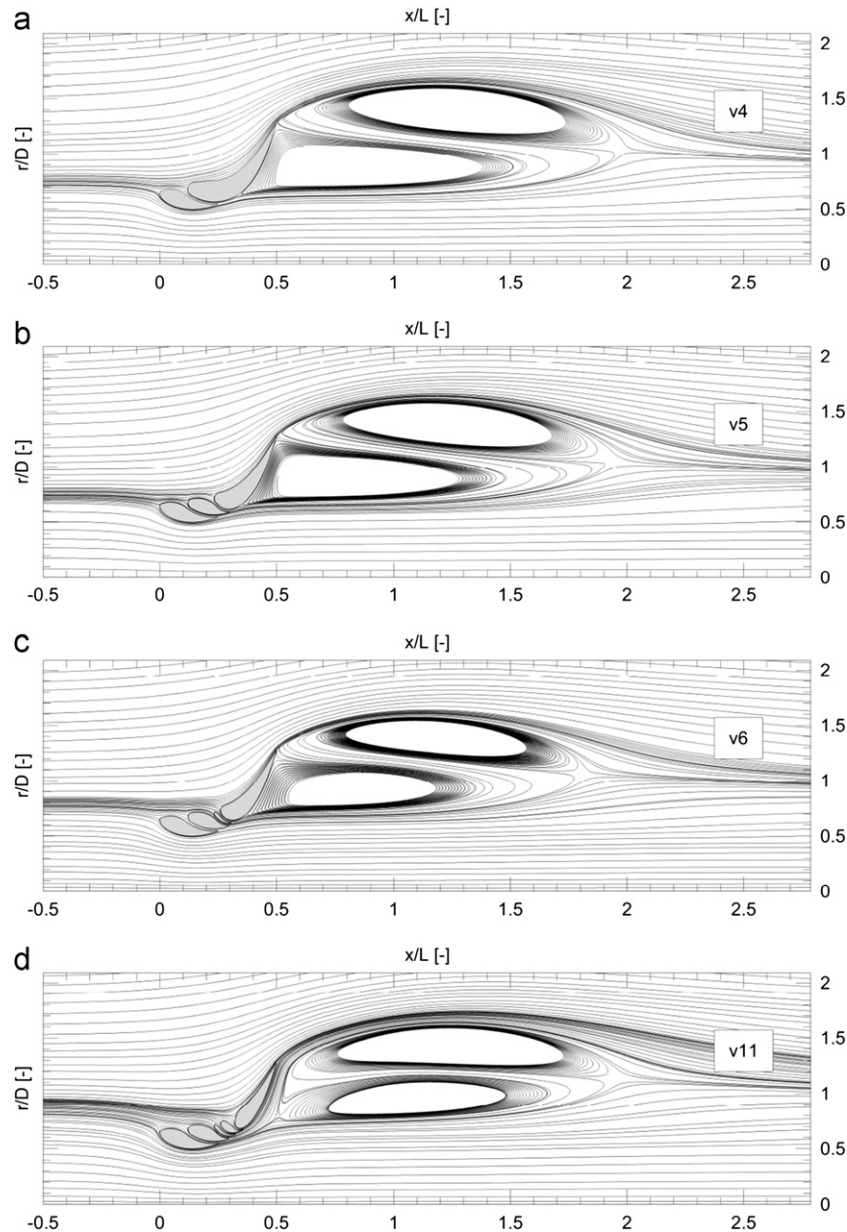


Fig. 13. Streamlines around the selected casing.

volumetric flow rate (Q) in the throat as follows:

$$Q = \frac{1}{A} \int_A u \cdot dA \quad (7)$$

where A is the throat area and u is the local velocity magnitude.

For one-, two- and three-ring slots, the volumetric flow rate increase through the casing is not significant. Moreover, for the $v5$ version, which corresponds to a two-slot casing, the volumetric flow is slightly decreased with respect to the previous versions. Thus, for the $v4$, $v5$ and $v6$ casings, the ratios between the volumetric flow rate that passes through the casing and the volumetric flow rate (Q_i) computed with the throat cross-section and the velocity at the inlet boundary of the computational domain are 2.01, 1.98 and 2.04, respectively.

For the $v11$ version, the volumetric flow rate increases with a ratio equal to 2.75, i.e., a mean value of 9.62 m/s for the velocity magnitude in the throat.

From the analysis of the numerical simulations carried out for the first three configurations, it is clear that the air injected

through the slots ensures the control of the main current separation and leads to a slight increase in the volumetric flow rate. The slots ensure an energy supplement that is mainly dissipated by the ring vortices, thereby maintaining the energy of the main flow through the casing.

For the fourth configuration, the volumetric flow rate through the casing is approximately 30% larger than that of the first three configurations, thus leading to a significant increase of the air velocity in the throat of the nozzle. These significant results are due to the consistent air intake injected through the fourth ring slot that, together with the air injected through the first three slots, creates an air ring current with an increased flow rate and a mean velocity that leads to flow attachment via the Coanda effect at the interior walls of the casing in the flared zone. This Coanda effect leads to a secondary ejection effect of the Coanda type with decisive consequences for the flow increase through the casing and thus for the velocity in the throat of the nozzle.

The dimensionless velocity magnitude contours around the studied casing versions are presented comparatively in Fig. 14.

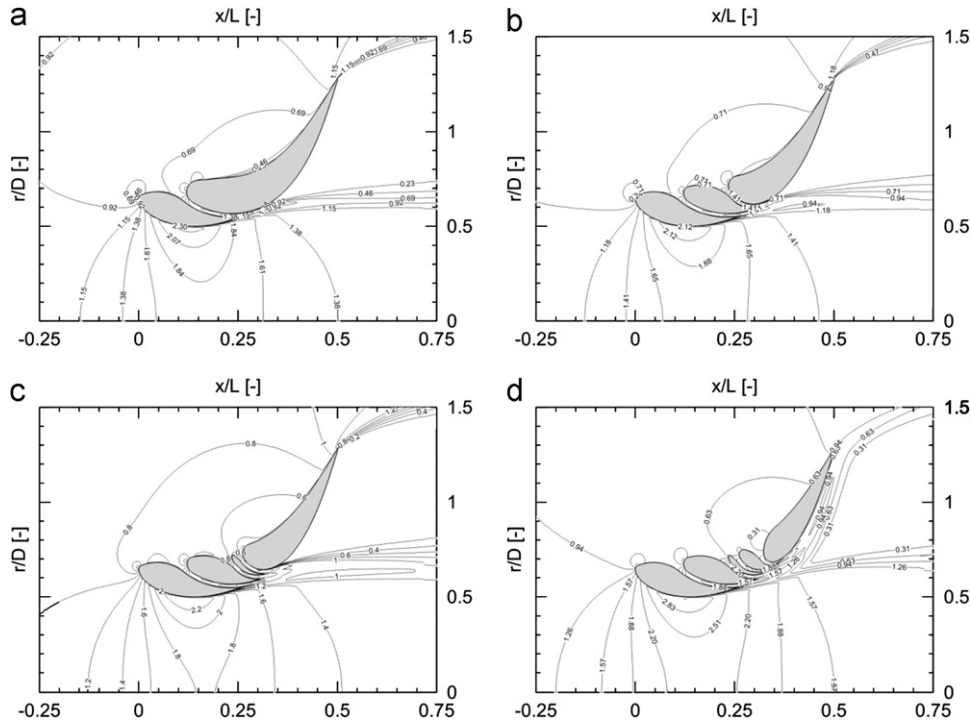


Fig. 14. Dimensionless velocity magnitude contours around the selected casing versions.

The velocity magnitude values are closely correlated to the volumetric flow rate values. The maximum values are obtained in the throat of the casing near the walls due to the intensification of the flow on the profiled boundary. For the $v4$ casing, the maximum velocity magnitude in the throat indicates an increase with respect to the free stream velocity by a factor of 2.37. In the case of the $v5$ and $v6$ versions, the maximum dimensionless velocity magnitude values are 2.33 and 2.40, respectively. The $v11$ casing ensures a maximum axial velocity increase in the active transversal section of the casing by a factor of 3.25.

The pressure coefficient contours around the selected casings are presented in Fig. 15. We observe that as the number of channels increases, the static pressure in the throat of the casing is decreased. However, there is an exception for the $v5$ casing equipped with two injection slots. The difference between the $v4$ and $v5$ versions is quite small, and that difference may be linked to the slight increase in velocity for the $v4$ casing compared to the $v5$ version. For the versions with one, two and three channels, the minimum pressure coefficient in the throat is equal to -4.87 , -4.7 and -5.06 , respectively. For the $v11$ casing, the minimum pressure coefficient value is equal to -9.27 , the lowest value obtained in the performed numerical simulations.

To quantify the energetic aspects of the flow inside the casing, we have considered 22 transversal sections along the axial direction of the casings for which we have computed the mean values for the static, the dynamic and the total pressure as

$$\begin{aligned}\bar{p}_i &= \frac{1}{A_i} \int_{A_i} p \cdot dA \\ \bar{p}_{di} &= \frac{1}{A_i} \int_{A_i} p_d \cdot dA \\ \bar{p}_{ti} &= \frac{1}{A_i} \int_{A_i} p_t \cdot dA\end{aligned}\quad (8)$$

where \bar{p}_i , \bar{p}_{di} and \bar{p}_{ti} are the mean values for the static pressure, the dynamic pressure and the total pressure in section i characterized by a transversal area A_i and in which p , p_d and p_t are the local values for the static, the dynamic and the total pressure, respectively.

The corresponding mean static, dynamic and total pressure coefficients were computed using those values:

$$\begin{aligned}C_{ps} &= (\bar{p} - p_\infty) / (0.5 \rho u_\infty^2) \\ C_{pd} &= (\bar{p}_d - p_\infty) / (0.5 \rho u_\infty^2) \\ C_{pt} &= (\bar{p}_t - p_\infty) / (0.5 \rho u_\infty^2)\end{aligned}\quad (9)$$

The variations of the pressure coefficients with respect to the dimensionless length of the casing are presented in Fig. 16. One can observe that for one-, two- and three-ring slots (Fig. 16(a), (b) and (c)), the kinetic energy (i.e., the dynamic pressure coefficients) increase through the casings does not vary significantly. Moreover, for the $v5$ version, the kinetic energy is slightly decreased when compared to that of the $v4$ version. Although the variations in the total pressure coefficients are influenced by the point at which the second separation of the main flow occurs, the values at the inlet and the outlet sections of the casing are similar for these three cases. In contrast, for the $v11$ version equipped with four circular slots, the kinetic energy increase is quite obvious (Fig. 16(d)). As the total pressure variation graph shows, the energy losses in the $v11$ casing are small when compared to previous versions, and this result occurs mainly due to flow reattachment after the last injection slot.

For a better comparison, Fig. 17 shows the pressure coefficient variations as a function of the dimensionless length for the initial $v-1$ casing. For this particular version, we have considered 42 transversal sections along the axial direction of the casing where we computed the mean values for the static, the dynamic and the total pressure.

We can observe that this initial version offers a performance similar to that of versions $v4$, $v5$ and $v6$. The volumetric flow increase ratio of the initial version has a value of 1.99, which does not differ substantially from that of the three casings presented in versions $v4$, $v5$ and $v6$. This observation leads to the conclusion that the existence of a boundary layer separation point on the interior surface of the case creates the conditions for the energy consumption from the main flow necessary to maintain the ring vortices.

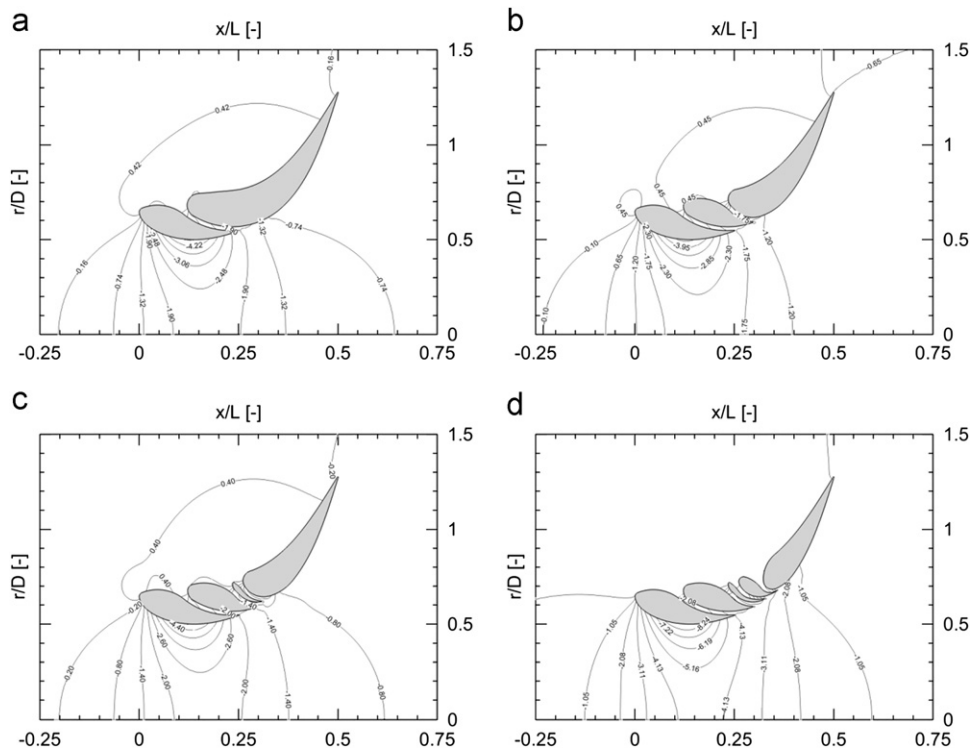


Fig. 15. Pressure coefficient contours around the selected casing versions.

In the *v11* version, the energy that maintains the downstream vortices is extracted from the injected flow from the exterior of the casing. The injected air is directed in a favorable manner due to the flow attachment via the Coanda effect at the interior wall of the casing in the flared zone.

5.2. Experimental investigation: $Re = 1.01 \times 10^5$

Using the numerically optimized *v11* casing, we performed an experimental study in the wind tunnel. Due to the wind tunnel limitations, the Reynolds number (computed with the diameter of the model throat) was set to 1.01×10^5 . After the experiment, a numerical simulation was also set up (as described in Section 2) using the geometry of the *v11* casing and modifying the inlet velocity boundary condition to obtain the same Reynolds number as that in the wind tunnel.

In Figs. 18 and 19, we present the pressure coefficient ($C_p = (p - p_\infty) / (0.5 \rho u_\infty^2)$) distributions on the interior surface of the casing and along the casing axis as measured in the experiment and compared to the numerical simulation results. In Fig. 18, for the pressure coefficient distributions resulting from numerical simulations, we have plotted only the values corresponding to the interior faces of the first and the fifth circular sections of the casing where the pressure taps are positioned in the experimental setup.

We observe that the main patterns of the pressure coefficient distributions obtained from both the numerical simulations and the experimental measurements are clearly in good agreement. For the first circular section, the results are well fitted, with a slight over-prediction of the pressure drop on the interior surface in the throat of the casing in the case of the numerical results. Downstream of the throat, both at the interior surface and on the axis, the numerical simulations over-predict the kinetic term recovery with pressure coefficient values larger than those resulting from the experiment.

One possible explanation for this result lies in the existence of the stiffening ribs on the experimental model that alter the flow

downstream of the throat. The effect given by this geometry (necessary for any real casing) was not considered in the 2D axisymmetric numerical simulations.

Another possible explanation is linked to the physical characteristics of the flow in the injection slots. The numerical simulation performed using the boundary conditions similar to conditions in the wind tunnel experiment suggests that the local Reynolds number in the channels (computed with the hydraulic diameter of the channel) varies between 4000 and 7000. The flow is therefore at the limit between a transitional and turbulent regime. The turbulence model adopted in the numerical simulations assumes that the flow is turbulent throughout the computational domain and is not able to predict the transition from a laminar to a turbulent regime. Thus, we believe that the numerical model may not be able to correctly predict the pressure drop in the ring slots. If this pressure drop is under-predicted, the air is injected into the main flow in the wind tunnel experiment at lower rates than those given by the numerical simulation. This occurrence would cause a smaller displacement of the separation point at the interior of the casing, which implies larger pressure losses in the casing and consequently a lower kinetic term recovery.

For this study, which aims to optimize the shape of the casing in terms of its axial length and the airflow that passes through the interior active transversal section, the differences between the numerical and experimental results were considered to be acceptable.

6. Conclusions

The aim of this study was to optimize the shape of a casing for a small wind turbine in terms of its axial length and of the volumetric flow rate that passes through the inner active transversal circular section where the turbine rotor will be mounted.

Numerical simulations were used as a tool in the process of obtaining an improved geometry for the casing. The numerical approach focused on a method that allows problem-solving in a

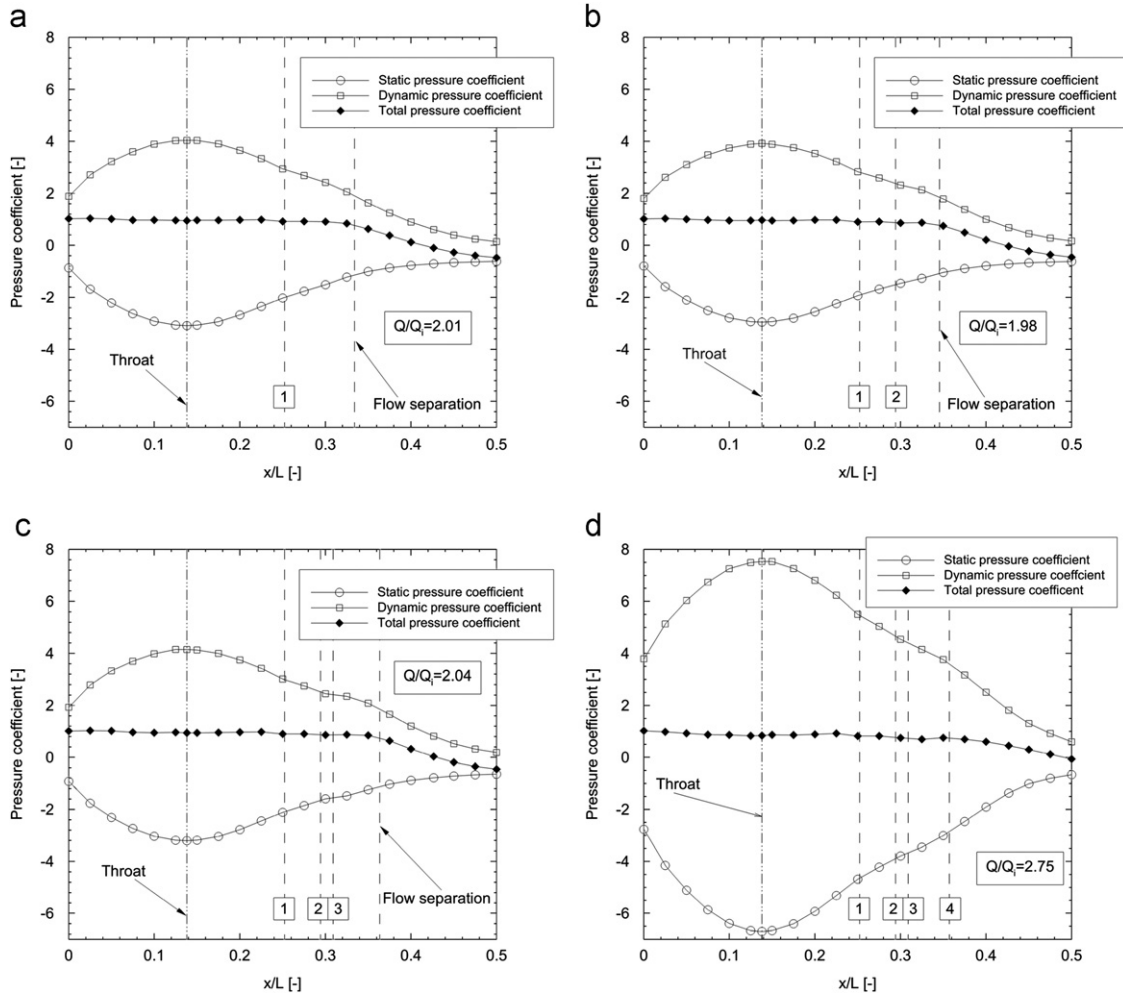


Fig. 16. Pressure coefficients as a function of the dimensionless length of the casing for the selected versions.

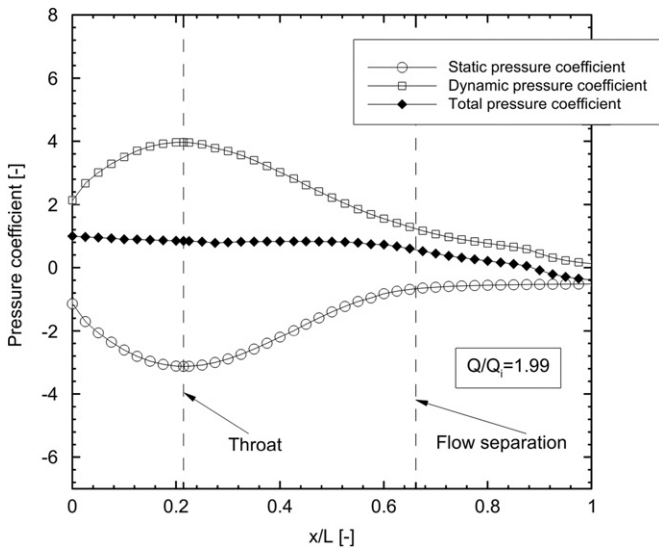


Fig. 17. Pressure coefficients as a function of the dimensionless length of the case for the v-1 version.

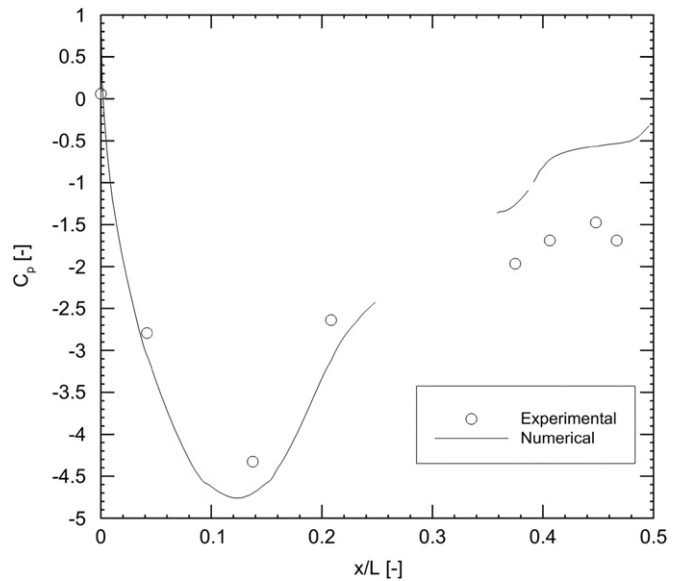


Fig. 18. Pressure coefficient distributions on the interior surface of the v11 1:20 scale model: experimental vs. numerical simulation comparison.

reasonably short computational time. The numerical method was tested using a well-documented test case from the literature similar to our study.

The numerical research presented in this paper leads to a casing shape that is characterized by a reduced axial dimension and by an important increase in the volumetric flow rate, which implies a

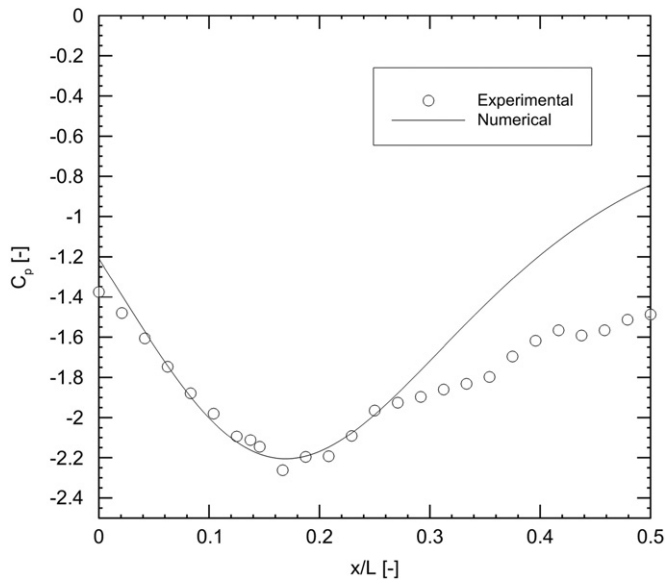


Fig. 19. Pressure coefficient distributions on the axis of the v11 1:20 scale model: experimental vs. numerical simulation comparison.

substantial increase in the air velocity in the rotor cross-section. The final shape of the casing equipped with a passive flow control device resulted at the end of an iterative heuristic optimization process. The optimization process led to numerical studies of thirteen casing versions, which corresponded to thirteen iteration steps in the procedure. The paper presents only four versions of the thirteen casings studied. The numerical results served to highlight how to ensure a better control over the separation of the main inner flow in the casing. The results also show how the air injection through the circular slots leads to an increase in the energy that will be further dissipated by the ring vortices located downstream of the casing.

For greater confidence in the results, basic experimental tests were also conducted. A 1:20 scale model of the final validated casing was built. From a qualitative point of view, the numerical and experimental results are in good agreement, both illustrating the same trends. From a quantitative point of view, the results are well fitted only for the zone upstream of the throat of the casing. Downstream of the throat, the numerical model over-predicts the kinetic term recovery. The main reasons for this over-prediction lies in the transitional flow regime that may occur in the injection slots of the experimental model (and cannot be predicted by the adopted numerical model) and in the existence of the stiffening ribs of the experimental model that alter the 2D axisymmetric hypothesis of the numerical model.

The performance of the validated casing must be further studied both with a 3D numerical model under transient conditions (i.e., with a turbulence model that is able to predict the transition from a laminar to a turbulent flow) and with an experimental model on a larger geometric scale that will permit a more accurate assessment of the flow regime in the circular slots. As a result of this process, the shape of the concentrator may be slightly changed.

Acknowledgments

The authors acknowledge the support from the Executive Unit for Financing of the Higher Education, Research, Development and

Innovation Grants (UEFISCDI PN-II PD-193 105/2010). All numerical simulations and experiments have been performed in the Hydraulics and Environmental Protection Department at the Technical University of Civil Engineering of Bucharest.

References

- Abe, K., Nishida, M., Sakurai, A., Ohya, Y., Kihara, H., Wada, E., Sato, K., 2005. Experimental and numerical investigations of flow fields behind a small wind turbine with a flanged diffuser. *Journal of Wind Engineering and Industrial Aerodynamics* 93, 951–970.
- Abe, K., Ohya, Y., 2004. An investigation of flow fields around flanged diffusers using CFD. *Journal of Wind Engineering and Industrial Aerodynamics* 92, 315–330.
- ANSYS Inc. 2010. *Fluent 13.0 Users Guide*.
- Bardina, J.E., Huang, P.G., Coakley, T.J., 1997. Turbulence modeling validation, testing and development. NASA Technical Memorandum, 110446.
- Bet, F., Grassmann, H., 2003. Upgrading conventional wind turbines. *Renewable Energy* 28, 71–78.
- Burt, M., 1994. A Selection of Experimental Test Cases for the Validation of CFD Codes: Chapter 5—Summaries of the Test Cases, AGARD AR-303, p.1.
- Coşoiu, C.I., Damian, R.M., Degeratu, M., Georgescu, A.M., Hlevca, D., Numerical study on the efficiency between the ducted and the free stream rotor of a horizontal axis wind turbine. In: *Proceedings of the EWEA 2011 Conference*, 14–17 March 2011, Brussels, Belgium.
- Davenport, A.G., Mackey, S., Melbourne, W.H., 1980. Tall Building criteria and loading, Chapter CL-3, Wind loading and wind effects. American Society of Civil Engineers, ISBN: 0-87262-237-1.
- Degeratu, M., Georgescu, A., Bandoc, G., Dumitru, G., 2003. Wind energy potential in the Romanian Black Sea coast area. In: *Proceedings of the International Conference on Energy and Environment—CIEM 2003*, Romanian Academy, vol 1, S1, pp. 1–6 (in Romanian).
- Fejtek, I., 1997. Summary of code validation results for a multiplelement airfoil test case. AIAA, 97–1932.
- Gilbert, B.L., Foreman, K.M., 1983. Experiments with a diffuser-augmented model wind turbine. *Journal of Energy Resources Technology—Transactions of the ASME* 105, 46–53.
- Gilbert, B.L., Oman, R.A., Foreman, K.M., 1978. Fluid dynamics of diffuser-augmented wind turbines. *Journal of Energy* 2 (6), 368–374.
- Igra, O., 1981. Research and development for shrouded wind turbines. *Energy Conversion and Management* 21, 13–48.
- Lilley, G.M., Rainbird, W.J., 1956. A Preliminary Report on the Design and Performance of Ducted Windmills. Report No. 102, College of Aeronautics, Cranfield, England.
- Matsushima, T., Takagi, S., Muroyama, S., 2006. Characteristics of a highly efficient propeller type small wind turbine with a diffuser. *Renewable Energy* 31 (9), 1343–1354.
- Menter, F.R., 1994. Two-equation eddy-viscosity turbulence models for engineering applications. *AIAA Journal* 32 (8), 1598–1605.
- Morrison, J.H., 1998. Numerical Study of Turbulence Model Predictions for the MD 30P/30N and NHP-2D Three Element Highlift Configurations, NASA report NASA/CR-1998-208967.
- Oertel, H., 2010. Prandtl-Essentials of Fluid Mechanics, 3rd Edition SpringerLink <http://dx.doi.org/10.1007/978-1-4419-1564-1>. (pp. 222–233).
- Ohya, Y., Karasudani, T., Sakurai, A., Abe, K., Inoue, M., 2008. Development of a shrouded wind turbine with a flanged diffuser. *Journal of Wind Engineering and Industrial Aerodynamics* 96, 524–539.
- Ohya, Y., Karasudani, T., Nagai, T., Uchida, T., Matsuura, C.T., Griffiths, H., 2011. Development of shrouded wind turbines with wind-lens technology. In: *Proceedings of the EWEA 2011 Conference*, 14–17 March 2011, Brussels, Belgium.
- Phillips, D.G., Flay, R.G.J., Nash, T.A., 1999. Aerodynamic analysis and monitoring of the Vortec 7 diffuser augmented wind turbine. In: *IPENZ Transactions*, vol. 26(1), Auckland, New Zealand, pp. 13–19.
- Pumpelly, R., 1905. Explorations in Turkestan with an Account of the Basin of Eastern Persia and Sistan. Expedition of 1903 under the Direction of Raphael Pumpelly, vol. 1. Carnegie Institute of Washington, Washington D.C..
- Rumsey, C.L., Gatski, T.B., Ying, S.X., Bertelrud, A., 1998. Prediction of high-lift flows using turbulent closure models. *AIAA Journal* 36 (5).
- Susan-Resiga, R.F., Muntean, S., Avellan, F., Anton, I., 2011. Mathematical modeling of swirling flow in hydraulic turbines for the full operating range. *Applied Mathematical Modeling* 35, 4759–4773.
- Wang, F., Bai, L., Fletcher, J., Whiteford, J., Cullen, D., 2008. The methodology for aerodynamic study on a small domestic wind turbine with scoop. *Journal of Wind Engineering and Industrial Aerodynamics* 96, 1–24.